

Surface growth effects on reactive capillary-driven flow: Lattice Boltzmann investigation

Danilo Sergi, Loris Grossi, Tiziano Leidi, and Alberto Ortona

University of Applied Sciences (SUPSI), The iCIMS Research Institute, Galleria 2, CH-6928 Manno, Switzerland

(Dated: November 15, 2021)

The Washburn law has always played a critical role for ceramics. In the microscale, surface forces take over volume forces and the phenomenon of spontaneous infiltration in narrow interstices becomes of particular relevance. The Lattice Boltzmann method is applied in order to ascertain the role of surface reaction and subsequent deformation of a single capillary in 2D for the linear Washburn behavior. The proposed investigation is motivated by the problem of reactive infiltration of molten silicon into carbon preforms. This is a complex phenomenon arising from the interplay between fluid flow, the transition to wetting, surface growth and heat transfer. Furthermore, it is characterized by slow infiltration velocities in narrow interstices resulting in small Reynolds numbers that are difficult to reproduce with a single capillary. In our simulations, several geometric characteristics for the capillaries are considered, as well as different infiltration and reaction conditions. The main result of our work is that the phenomenon of pore closure can be regarded as independent of the infiltration velocity, and in turn a number of other parameters. The instrumental conclusion drawn from our simulations is that short pores with wide openings and a round-shaped morphology near the throats represent the optimal configuration for the underlying structure of the porous preform in order to achieve faster infiltration. The role of the approximations is discussed in detail and the robustness of our findings is assessed.

Keywords: Capillary infiltration; Surface growth; Lattice Boltzmann simulation; Liquid silicon infiltration

1. Introduction

The infiltration of porous carbon (C) by molten silicon (Si) is a widespread industrial technique for the fabrication of composite materials with enhanced thermal and mechanical resistance at high temperatures (Hillig et al., 1975). Central to this process are of course the wetting properties of the substrate against molten Si. Importantly, it appears that capillary forces are strongly affected by the reactivity at high temperatures between Si and C to form silicon carbide (SiC). A large body of research has been devoted to the subject, definitely defying conventional modeling (Dezellus and Eustathopoulos, 2010; Dezellus et al., 2003; Mortensen et al., 1997) and experimental (Eustathopoulos et al., 1999) approaches. The interested reader can find more details about the experimental work in Liu et al. (2010) and references therein. Our simulations are based on the Lattice Boltzmann (LB) method (Benzi et al., 1992; Succi, 2009; Sukop and Thorne, 2010). For advanced capillary problems, the accuracy of this numerical scheme for hydrodynamics has been proven to be comparable with the well-established method of Computational Fluid Dynamics (CFD) relying on finite elements (Chibbaro et al., 2009b). Here we deal with the ability of the LB method to address the dynamic behavior of capillary infiltration coupled to surface growth. Of special interest is the retardation induced to the Washburn law by the dynamic reduction in pore radius. More generally, the present work can help to understand experimental results carried out with Si alloys (Bougiouri et al., 2006; Calderon et al., 2010a; Sangsuwan et al., 1999; Voytovych et al., 2008). Precisely, the focus is on the linear Washburn law for a single capillary in 2D (Chibbaro, 2008; Chibbaro et al., 2009a). This behavior is typical for the infiltration of pure Si in carbon preforms (Israel et al., 2010). Furthermore, the Washburn analysis for bulk structures is based on the results for a single capillary (Einset, 1996 and 1998). In the LB model, the surface reaction is treated as a precipitation process from supersaturation (Bougiouri et al., 2006; Calderon et al.,

2010a and 2010b; Kang et al., 2007, 2003, 2002b, 2004; Lu et al., 2009). It is also worth mentioning the article by Miller and Succi (2002) as pioneering work using the LB method for this subject. Our simulations indicate that the thickening of the surface behind the contact line actually limits the infiltration process. This phenomenon is especially marked in the vicinity of the onset of pore closure. For this reason, we argue that the effect of retardation is stronger when surface growth inside narrow interstices obstructs the flow (here the wetting transition at the contact line is neglected (Calderon et al., 2010b; Dezellus et al., 2005; Voytovych et al., 2008)). Importantly, it arises that higher infiltration velocities, achieved for example by tuning some parameters defining the capillary geometry, have little to no influence on the process of pore closure by surface reaction. It follows that the distribution of pore size is a critical parameter for reactive capillary infiltration, besides other aspects to be discussed in the sequel. The engineering problem under consideration is an involved process arising from the mutual dependence between various phenomena. Unavoidably, our description suffers from several simplifications. We also verify that our findings remain robust under the existing approximations.

2. Computational models

The distinctive feature of the LB method resides in the discretization of the velocity space: only a finite number of elementary velocity modes is available. Locally, the movement of the fluid particles along a particular direction is accounted for statistically by means of distribution functions, in terms of which the intervening physical quantities are expressed. Hydrodynamic behavior is recovered in the limit of small Mach numbers, corresponding to the incompressible limit (Chen and Doolen, 1998). It has been shown that the problem of capillary flow is better described by a multicomponent system (Kang et al., 2002a; Shan and Chen, 1993; Shan and Doolen,

1995), since allowing to reduce the evaporation-condensation effect (Chibbaro, 2008; Chibbaro et al., 2009a; Diotallevi et al., 2009a and 2009b; Pooley et al., 2009). On a d2q9 lattice, the evolution of every single fluid component is obtained by iterating the BGK equation (Bhatnagar et al., 1954)

$$f_i^\sigma(\mathbf{r} + \mathbf{e}_i \Delta t, t + \Delta t) = f_i^\sigma(\mathbf{r}, t) - \frac{1}{\tau_\sigma} [f_i^\sigma(\mathbf{r}, t) - f_i^{\sigma, \text{eq}}(\rho_\sigma, \mathbf{u}_\sigma^{\text{eq}})] \quad i = 0 - 8. \quad (1)$$

The lattice spacing is denoted by Δx and the time increment by Δt ; hereafter, without loosing generality $\Delta x = \Delta t = 1$ (in model units). The f_i^σ 's are the distribution functions for the velocity modes \mathbf{e}_i . The superscript $\sigma = 1, 2$ designates the substance. The discrete velocity modes are defined as follows

$$\mathbf{e}_i = \begin{cases} (0, 0) & i = 0 \\ (\cos[(i-1)\pi/2], \sin[(i-1)\pi/2]) & i = 1 - 4 \\ \sqrt{2}(\cos[(2i-9)\pi/4], \sin[(2i-9)\pi/4]) & i = 5 - 8. \end{cases}$$

The equilibrium distribution functions read

$$f_i^{\sigma, \text{eq}}(\rho_\sigma, \mathbf{u}_\sigma^{\text{eq}}) = w_i \rho_\sigma(\mathbf{r}, t) \left[1 + 3\mathbf{e}_i \cdot \mathbf{u}_\sigma^{\text{eq}} + \frac{9}{2}(\mathbf{e}_i \cdot \mathbf{u}_\sigma^{\text{eq}})^2 - \frac{3}{2}\mathbf{u}_\sigma^{\text{eq}} \cdot \mathbf{u}_\sigma^{\text{eq}} \right] \quad i = 0 - 8.$$

The coefficients w_i are defined as $w_0 = 4/9$, $w_i = 1/9$ for $i = 1 - 4$ and $w_i = 1/36$ for $i = 5 - 8$ (He and Luo, 1997; Wolf-Gladrow, 2005). The local density, ρ_σ , and the equilibrium velocity, $\mathbf{u}_\sigma^{\text{eq}}$, have the explicit form

$$\rho_\sigma(\mathbf{r}, t) = \sum_{i=0}^8 f_i^\sigma(\mathbf{r}, t)$$

$$\mathbf{u}_\sigma^{\text{eq}}(\mathbf{r}, t) = \mathbf{u}'(\mathbf{r}, t) + \frac{\tau_\sigma \mathbf{F}_\sigma(\mathbf{r}, t)}{\rho_\sigma(\mathbf{r}, t)}.$$

\mathbf{F}_σ is the resultant force experienced by the fluid component σ . The velocity \mathbf{u}' is given by

$$\mathbf{u}' = \left(\sum_\sigma \frac{\rho_\sigma(\mathbf{r}, t) \mathbf{u}_\sigma(\mathbf{r}, t)}{\tau_\sigma} \right) / \sum_\sigma \frac{\rho_\sigma(\mathbf{r}, t)}{\tau_\sigma},$$

where we have introduced the σ -th component fluid velocity

$$\mathbf{u}_\sigma(\mathbf{r}, t) = \frac{1}{\rho_\sigma(\mathbf{r}, t)} \sum_i f_i^\sigma(\mathbf{r}, t) \mathbf{e}_i.$$

The velocity \mathbf{u}' satisfies the requirement of momentum conservation in the absence of external forces (Kang et al., 2002a; Shan and Chen, 1993; Shan and Doolen, 1995). In Eq. 1, τ_σ is the relaxation time, determining the kinematic viscosity $\nu_\sigma = (2\tau_\sigma - 1)/6$. The dynamic viscosity is defined as (Chibbaro, 2008)

$$\mu = \rho \nu = \sum_\sigma \mu_\sigma = \sum_\sigma \rho_\sigma \nu_\sigma.$$

The total density of the whole fluid is of course $\rho = \sum_\sigma \rho_\sigma$. Collisions between the liquid phase and the solid boundaries

are treated according to the common bounce-back rule, implementing the no-slip condition for rough surfaces. Cohesive forces in the liquid phase are evaluated by means of the formula (Martys and Chen, 1996)

$$\mathbf{F}_{c, \sigma}(\mathbf{r}, t) = -G_c \rho_\sigma(\mathbf{r}, t) \sum_{i=1}^8 w_i \rho_{\bar{\sigma}}(\mathbf{r} + \mathbf{e}_i \Delta t, t) \mathbf{e}_i;$$

$\bar{\sigma}$ being the other fluid component with respect to σ . The parameter G_c determines the interaction strength. Adhesive forces between the liquid and solid phases are computed using the formula (Martys and Chen, 1996)

$$\mathbf{F}_{\text{ads}, \sigma}(\mathbf{r}, t) = -G_{\text{ads}, \sigma} \rho_\sigma(\mathbf{r}, t) \sum_{i=1}^8 w_i s(\mathbf{r} + \mathbf{e}_i \Delta t, t) \mathbf{e}_i.$$

The interaction strength is adjusted via the parameter $G_{\text{ads}, \sigma}$. The function s takes on the value 1 if the velocity mode \mathbf{e}_i points to a solid node, otherwise it vanishes.

The LB scheme can encompass convection-diffusion systems readily under the assumption of low concentrations. This condition implies that fluid flow is not affected by molecular diffusion. Solute transport is described by introducing the distribution functions g_i . For solute transport we use the d2q4 lattice (Kang et al., 2007), generally applied also for thermal fields (Mohamad et al., 2009; Mohamad and Kuzmin, 2010). The reduced number of degrees of freedom does not restrain the predictive capacity of the model (Wolf-Gadrow, 1995). As for fluid flow, the evolution follows the BGK equation (Kang et al., 2007, 2003, 2002b, 2004; Lu et al., 2009)

$$g_i(\mathbf{r} + \mathbf{e}_i \Delta t, t + \Delta t) = g_i(\mathbf{r}, t) - \frac{1}{\tau_s} [g_i(\mathbf{r}, t) - g_i^{\text{eq}}(C, \mathbf{u})] \quad i = 1 - 4.$$

The relaxation time for solute transport is denoted τ_s , defining the diffusion coefficient $D = (2\tau_s - 1)/4$ (Kang et al., 2007). For the d2q4 lattice, the equilibrium distribution functions take the form (Kang et al., 2007)

$$g_i^{\text{eq}}(C, \mathbf{u}) = \frac{1}{4} C [1 + 2\mathbf{e}_i \cdot \mathbf{u}] \quad i = 1 - 4. \quad (2)$$

The solute concentration is given by $C = \sum_i g_i$. The local solvent velocity \mathbf{u} is assumed to be the overall fluid velocity (Kang et al., 2002a; Shan and Chen, 1993; Shan and Doolen, 1995)

$$\mathbf{u}(\mathbf{r}, t) = \left(\sum_\sigma \left[\rho_\sigma(\mathbf{r}, t) \mathbf{u}_\sigma(\mathbf{r}, t) + \frac{1}{2} \mathbf{F}_\sigma(\mathbf{r}, t) \right] \right) / \sum_\sigma \rho_\sigma(\mathbf{r}, t).$$

It may be useful to have interfaces also for solute transport in order to prevent diffusion from the liquid to the vapor phase. In analogy with multiphase fluid flow (Shan and Chen, 1993 and 1994), we add to the velocity \mathbf{u} in Eq. 2 a term of the form $\tau_s \mathbf{F}_s / C$. The function \mathbf{F}_s is defined as

$$\mathbf{F}_s(\mathbf{r}, t) = -G_s \varphi(\mathbf{r}, t) \sum_{i=1}^4 \varphi(\mathbf{r} + \mathbf{e}_i \Delta t, t) \mathbf{e}_i. \quad (3)$$

The parameter G_s allows to tune the intensity. The function $\varphi(\mathbf{r}, t)$ is given by

$$\varphi(\mathbf{r}, t) = \varphi_0 e^{-C_0/C(\mathbf{r}, t)}.$$

This mechanism introduces an interface acting as a barrier to diffusion moving with the overall fluid. Far from interfaces, \mathbf{F}_s vanishes and diffusive transport is restored. The contribution of \mathbf{F}_s is taken into account also for the nodes belonging to the surface of the solid phase.

At the reactive boundary, the solute concentration C satisfies the macroscopic equation (Kang et al., 2007, 2003, 2002b, 2004; Lu et al., 2009)

$$D \frac{\partial C}{\partial n} = k_r (C - C_s),$$

where k_r is the reaction-rate constant and C_s the saturated concentration. From the constraint of the above equation, it is possible to calculate the solute concentration at the solid-liquid interface (Kang et al., 2007)

$$C = \frac{2g_{\text{out}} + k_r C_s}{k_r + 1/2},$$

where g_{out} is the distribution function of the modes leaving the fluid phase. At the solid boundaries, the distribution functions g_{in} for the modes e_i pointing in the fluid phase remain undetermined. They are updated according to the rule $g_{\text{in}} = -g_{\text{out}} + C/2$; g_{in} and g_{out} are associated with opposite directions. As time goes on, solute mass deposits on the reacting solid surface. The mass is updated iterating the equation (Kang et al., 2004; Lu et al., 2009)

$$b(\mathbf{r}, t + \Delta t) = b(\mathbf{r}, t) + k_r (C - C_s).$$

We indicate by b_0 the initial mass present on solid boundaries. The solid surface grows whenever $b(\mathbf{r}, t)$ exceeds the threshold value b_{max} . The new solid node is chosen with uniform probability among the surrounding nodes belonging to the liquid phase. Only direct neighbors are taken into account. The cumulated mass of the solid node that triggered surface growth is set to zero.

Lattice Boltzmann simulations process and output data in model units. The different quantities will be expressed in terms of the basic model units for mass, length and time, denoted by μ , lu and ts , respectively. Direct comparison with physical systems is possible after suitable transformations (Lu et al., 2009). This procedure is not strictly necessary since, in order to describe properly the real systems, it is sufficient to have the same Reynolds number Re for fluid flow (Landau and Lifshitz, 2008), and the same Damkohler number Da and supersaturation ψ for solute transport (Kang et al., 2003 and 2004; Lu et al., 2009). These dimensionless parameters are the same in LB and physical units, expressed for example in the common SI system or the Gauss system. For the reactive infiltration of molten Si in a capillary of $10 \mu\text{m}$ in width, the Reynolds number can be estimated to be $Re \approx 10^{-6}$ (Einset, 1996; Voytovych et al., 2008). This Reynolds number asks for extreme simulation conditions that can not be achieved. Indeed, a channel of width 50 lu using $\tau_\sigma = 1 \text{ ts}$ would require a

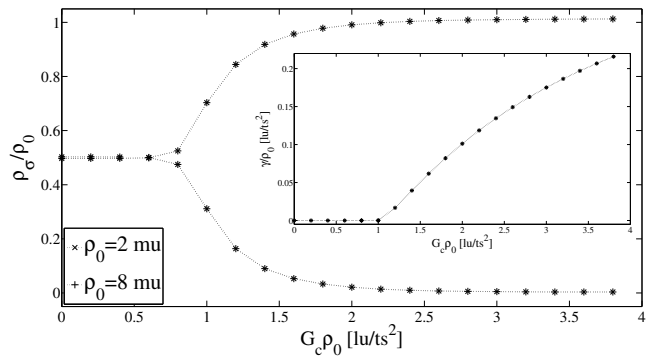


Figure 1: Scaled density ρ_σ/ρ_0 as a function of $G_c \rho_0$. The upper branch corresponds to ρ_1/ρ_0 inside the bubble (main density), while the lower branch is ρ_2/ρ_0 (dissolved density). Inset: Dependence of the scaled surface tension γ/ρ_0 on $G_c \rho_0$. The results of the simulations are averaged over the last 10 frames.

velocity of infiltration $u \approx 10^{-8} \text{ lu/ts}$. Thus, in the following, it should be borne in mind that our simulations significantly overestimate the typical Reynolds numbers for the problem at hand. In other words, this means that the process of infiltration is too fast. This numerical deficiency is partly reduced by the fact that the precipitation process from supersaturation should not have a strong dependence from the velocity of the invading front (Kang et al., 2003 and 2004; Lu et al., 2009).

3. Results and Discussion

3.1 Interfaces and surface tension

Cohesive forces among molecules of the same species have the effect to give rise to interfaces separating the fluid components. Given two immiscible fluids, the work necessary in order to deform the interface of area A is $\delta W = \gamma dA$, where γ is the surface tension. By taking into account the work of pressure forces, the condition of mechanical equilibrium leads to Laplace law (de Gennes et al., 2004; Kang et al, 2002a)

$$\Delta P = \frac{\gamma}{r} \quad \text{in 2D.} \quad (4)$$

In the above formula, r is the radius of the spherical droplet. The pressure drop across the interface has the explicit form $\Delta P = P_{\text{in}} - P_{\text{out}}$, with self-explanatory notation. In order to understand the interplay between interfacial tension, wetting and capillary flow, we first consider the formation of stable droplets for systems containing two fluid components. The size of the simulation domain is $N_x \times N_x$ with $N_x = 200 \text{ lu}$; periodic boundary conditions are applied. In the center is placed a droplet of fluid 1 immersed in fluid 2. Inside the bubble, ρ_1 is the main density and ρ_2 is the dissolved density. For the initial condition, we assume that $\rho_2/\rho_1 = 2.5\%$ and outside the bubble their values are inverted. The initial total density is denoted by $\rho_0 = \rho_1 + \rho_2$. By choosing the initial radius of the droplet to be $r = N_x/\sqrt{2\pi}$, it follows that both fluids have equal total masses, as assumed by Huang et al. (2007). The

densities of both fluids determine the pressure P . Let ρ_1 and ρ_2 be the densities of fluids 1 and 2 at point $\mathbf{r} = (x, y)$, then the pressure is given by (Huang et al., 2007; Shan and Chen, 1993; Shan and Doolen, 1995)

$$P(\mathbf{r}) = \frac{\rho_1(\mathbf{r}) + \rho_2(\mathbf{r})}{3} + \frac{G_c}{3} \rho_1(\mathbf{r}) \rho_2(\mathbf{r}). \quad (5)$$

In Eq. 4, for P_{in} we use the value obtained by averaging over a square of side length $2L_0 + 1$ centered in the simulation domain; $L_0 = 20$ lu. Instead, for P_{out} , the average is taken over the square $[0, 2L_0 + 1] \times [0, 2L_0 + 1]$. Every dynamics amounts to 100'000 timesteps. For the analysis, 50 uniformly-spaced frames are collected. In order to derive the radius of the droplets, it is necessary to determine the location of the interface separating the fluid components. To do this, we start from the point $(0, N_y/2)$ and consider at every step points incremented by one unit in x , i.e. $x \rightarrow x + 1$, applying every time the following rules. If $\rho_1(x+1)/\rho_1(x) > 1.05$ holds, it follows that the density for the first fluid increases at least of 5% in passing from x to $x + 1$. We consider these lattice sites as belonging to the interface. For this set of points, we determine x_{max} and x_{min} and it is assumed that the interface has coordinates $x = (x_{\text{max}} + x_{\text{min}})/2$ and $y = N_y/2$. Figure 1 illustrates the results according to the analysis proposed by Huang et al. (2007). It turns out that the surface tension γ is appreciable only for $G_c \rho_0 > 1$, as thoroughly discussed by Huang et al. (2007). We consider outliers the two points for which $G_c \rho_0 \leq 1$ and exhibiting a weak phase separation (broad interface), since inspection of the density values during the dynamics indicates that the systems are still evolving towards the equilibrium state after 100'000 timesteps. For $\rho_0 = 2$ mu/lu² and $G_c \rho_0 = 1$ lu/ts², the average over the last 20'000 timesteps for a simulation of 500'000 timesteps yields $\rho_1 = 1.17744$ mu/lu². For the shorter dynamics we obtained $\rho_1 = 1.40671$ mu/lu². Furthermore, there appears that, even for the longer simulation, the density values still exhibit systematic variations of at least 1% over the last 20'000 timesteps. It is thus clear that ρ_1/ρ_0 tends towards 0.5 (Huang et al., 2007). For 1'000'000 iterations this limit is further approached since $\rho_1 = 1.12514$ mu/lu². On the other hand, for $\rho_0 = 2$ mu/lu² and $G_c \rho_0 = 1.4$ lu/ts², we obtain $\rho_1 = 1.83668$ mu/lu² in the case of a long simulation. The results remain practically unchanged since for the shorter simulation we have $\rho_1 = 1.83733$ mu/lu² and the difference between the two corresponding values for the surface tension is on the order of 10^{-5} mu/lu². For systems with higher surface tension the convergence towards the equilibrium state is faster. In the following, we will concentrate ourselves on three particular values of surface tension, leading in general to consistent and quite accurate results.

3.2 Contact angle

The wetting behavior of a surface against a liquid is usually characterized via the equilibrium contact angle. Given the profile of the droplet, it is defined as the angle formed by the tangent at the contact line, that is, the edge where the

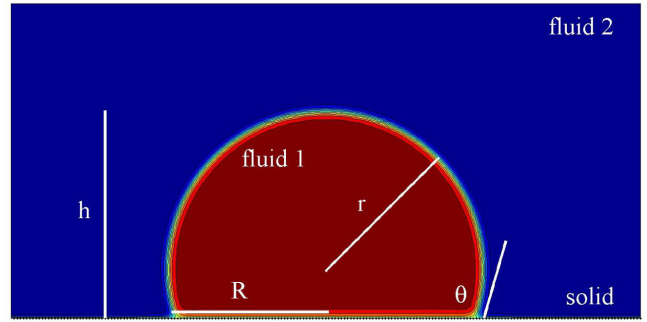


Figure 2: Sessile droplet system for the determination of the contact angle θ . The solid line is the tangent at the triple line. Color code based on density. h is the height, r the radius and R the base radius.

phases solid (S), liquid (L) and vapor (V) meet (see Fig. 2). For macroscopic, spherical droplets, Young equation (Young, 1805) relates the contact angle θ to the interfacial tensions γ_{ij} ($i, j = \text{S, L, V}$):

$$\cos \theta = \frac{\gamma_{\text{SV}} - \gamma_{\text{SL}}}{\gamma}.$$

For the solid-liquid surface tension we continue to use the simpler notation γ . If $\theta < 90^\circ$, the liquid wets the substrate (hydrophilic regime); otherwise, if $\theta > 90^\circ$, the substrate is hydrophobic.

In our simulations, the contact angle is determined using the sessile droplet method. The simulation domain is $N_x = 400$ lu long and $N_y = 200$ lu wide. The substrate coincides with the bottom of the simulation domain; the other boundaries are periodic. In the initial state, a square of side length 80 lu of the first fluid is centered in the simulation domain, placed in contact with the solid phase. The systems consist of a binary mixture where the droplet is represented by the wetting fluid immersed in the non-wetting component. As in Sec. 3.1, for the initial condition, $\rho_1/\rho_2 = 2.5\%$ with $\rho_0 = \rho_1 + \rho_2 = 2$ mu/lu². The simulations are performed with three different values for G_c . The equilibrium contact angle is varied by considering different values for the interaction parameters $G_{\text{ads}, \sigma}$. The evolution of the systems consists of 100'000 timesteps.

In the analysis, the contact angle is extracted using the method employed by Schmieschek and Harting (2011). In the micron scale, the droplet profile can be safely assumed to be spherical (Sergi et al., 2012). Here, our systems refer to millimeter-sized droplets (Bougiouri et al., 2006; Voytovych et al., 2008). So, let h be the height of the spherical cap and R the base radius (contact line curvature), then the radius and the contact angle can be written respectively as

$$r = \frac{h^2 + R^2}{2h} \quad \text{and} \quad \theta = \frac{\pi}{2} \mp \arccos\left(\frac{R}{r}\right),$$

for the hydrophilic ($R/h > 1$) and hydrophobic ($R/h < 1$) regimes, respectively. For clarity, these quantities are shown in Fig. 2. For the determination of the height and base radius of the droplets the interface between the wetting and non-wetting fluid is derived as explained in Sec. 3.1. An alternative way for calculating the contact angle is to use the formula

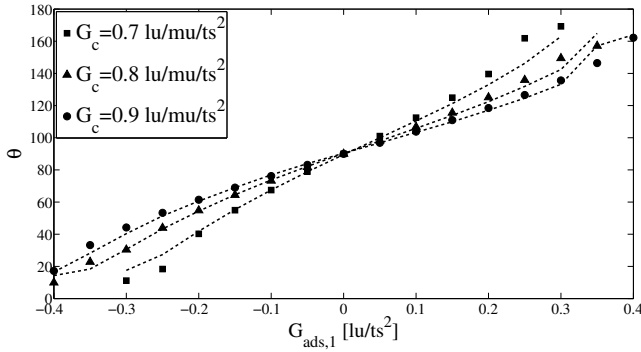


Figure 3: Dependence of the contact angle θ on the solid-liquid interaction parameter $G_{\text{ads},1} = -G_{\text{ads},2}$ for the simulation of the sessile droplet system (see Fig. 2). Three different surface tensions are considered by varying the parameter G_c (see Fig. 1). Points represent the results directly obtained from the profiles. The results predicted by Eq. 6 correspond to the dashed lines. The results of the simulations are averaged over the last 10 frames. The cases for which it is difficult to extract the contact angle are omitted.

(Huang et al., 2007)

$$\cos \theta = \frac{G_{\text{ads},2} - G_{\text{ads},1}}{G_c \frac{\rho_1 - \rho_2}{2}}. \quad (6)$$

ρ_1 and ρ_2 are the main and dissolved densities averaged over the region $[0, 2L_0 + 1] \times [0, 2L_0 + 1]$ with $L_0 = 5$ lu centered in the point $(N_x/2, h/2)$. Figure 3 plots the contact angle versus the interaction parameter controlling adhesive forces between the solid and liquid phases. As the surface tension increases, it appears that the agreement between the two approaches is more stringent. Our findings are in good accordance with those reported by Huang et al. (2007).

3.3 Capillary flow

Capillary flow occurs when a liquid spontaneously spreads inside a channel. This phenomenon was exhaustively modeled by Washburn and Lukas (Lukas, 1918; Washburn, 1921). It may be mentioned that historically capillarity played also an important role in the development of molecular theories (Israelachvili, 2011). For two fluids with the same density and dynamic viscosity, by taking into account inertial effects, the centerline position of the invading front $z(t)$ satisfies the differential equation (Szekely et al., 1971)

$$\frac{d^2 z(t)}{dt^2} + \frac{12\mu}{H^2 \rho} \frac{dz(t)}{dt} = \frac{2\gamma \cos \theta}{H \rho L}. \quad (7)$$

The first term on the left-hand side accounts for the inertial resistance and the second one for the viscous resistance. The term on the right-hand side is due to capillary forces. H and L are the height and length of the capillary. θ is the contact angle formed by the wetting fluid. Under the assumption of a constant contact angle, a solution of Eq. 7 is obtained by

(Chibbaro et al., 2009a)

$$z(t) = \frac{V_{\text{cap}} H \cos \theta}{6L} t_{\text{d}} [\exp(-t/t_{\text{d}}) + t/t_{\text{d}} - 1] + z_0. \quad (8)$$

The initial position of the interface is denoted by z_0 . $V_{\text{cap}} = \gamma/\mu$ is the capillary speed and $t_{\text{d}} = \rho H^2/12\mu$ is a typical transient time (Chibbaro et al., 2009a).

For times sufficiently large, Eq. 8 leads to $z(t) \propto t$ and the infiltration rate is given by $K = V_{\text{cap}} H \cos \theta/6L$. Thus, this model reproduces correctly the linear dependence of the displacement front with time observed for molten Si and some alloys in porous carbon (Bougiouri et al., 2006; Calderon et al., 2010a; Voytovych et al., 2008). Nevertheless, some hypothesis on which the result of Eq. 8 resides are not fulfilled in the experimental systems. For example, the liquid and vapor phases do not have approximately the same density. In the LB model, the density of both fluids determine the surface tension (see Eqs. 4 and 5). In the sequel, we will focus primarily on systems having an equilibrium contact angle around 30° (see Sec. 3.2). This result is consistent with the experimental results for molten Si and alloys on porous carbon substrates (Bougiouri et al., 2006; Voytovych et al., 2008). Instead, the hypothesis assuming the same viscosity for both fluids is more restricting. Indeed, the attempt to increase the ratio between the liquid and vapor phases in the LB model would result in a breakdown of the linear Washburn law (Chibbaro, 2008). In that respect, it is worthy of mention the fact that for Si alloys, without reaction, spontaneous infiltration does not even occur (Bougiouri et al., 2006). It follows that the present model only reproduces the macroscopic desired behavior and the effect of the reaction at the contact line is equivalent to the presence, in the capillary, of a second fluid as viscous as the wetting component. As a consequence, this means that the role of the surface reaction between Si and C to form SiC can not be reduced to a simple transition from a non-wetting to a wetting regime at the contact line of the invading front.

In order to give evidence of the behavior predicted by Eq. 8, we consider systems similar to that shown in Fig. 4. As before, the initial densities satisfy $\rho_1/\rho_2 = 2.5\%$ with $\rho_0 = \rho_1 + \rho_2 = 2$ mu/lu². The width of the capillary varies from 25 to 100 lu, corresponding to the height of the simulation domain. The length of the simulation domain is instead set initially to 1'000 lu. The length of the capillary is $L = 500$ lu. The left extremity of the capillary coincides with $x = 450$ lu. Every system is let evolve for 100'000 timesteps. The dynamics is studied by collecting 50 evenly-spaced frames. In the analysis of the data, we first track the invading front along the centerline of the capillary, by employing the method described in Sec. 3.1. The contact angle θ in Eq. 8 is derived from the capillary pressure using the formula $\Delta P = 2\gamma \cos \theta/H$ (Chibbaro, 2008; Chibbaro et al., 2009a). In this case, the pressures P_{in} and P_{out} are computed by averaging the pressure $P(r)$, Eq. 5, over regions of the type $[0, 2L_0 + 1] \times [0, 2L_0 + 1]$. These regions are centered around a point 20 lu apart from the centerline position of the meniscus in both the wetting and non-wetting fluids. It is assumed that $L_0 = 10$ lu. This procedure yields the most accurate matching between theory and simulation results (Chibbaro et al., 2009a), allowing also to avoid difficulties related

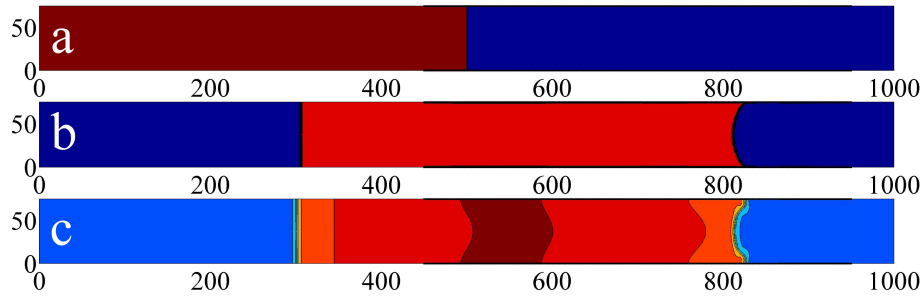


Figure 4: Set-up for the simulations of capillary-driven flow. Color code based on density: the first fluid is represented in red (high) and the second one in blue (low). Black points represent the solid boundary. The simulation domain has periodic boundary conditions. (a) Initial configuration. The first fluid fills the capillary along a distance of 50 lu. (b) State of the system after the formation of the meniscus and partial penetration. The flat interface guarantees that the first fluid can be regarded as forming an infinitely large phase, mimicking in this way a reservoir. (c) In this case the color code is based on solute concentration. The region filled with the first fluid is at a higher concentration and the dividing interface from the low-concentration region approximately coincides with the interface for fluid flow.

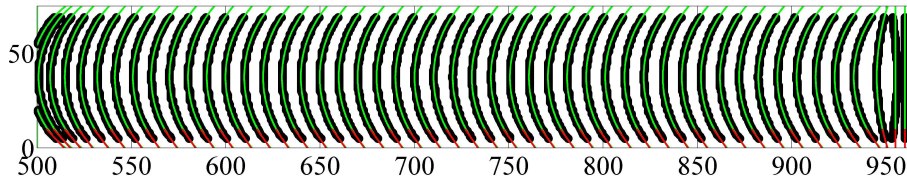


Figure 5: Infiltration front at different times. Black points represent the profile as obtained from simulations. The green line is a fit to the data using a circle as model function. The red straight line is the tangent at the point where the contact angle θ for the wetting fluid is determined. In general, the results determined in this way are in reasonable accordance with those based on capillary pressure (cf. Chibbaro et al. (2009b)).

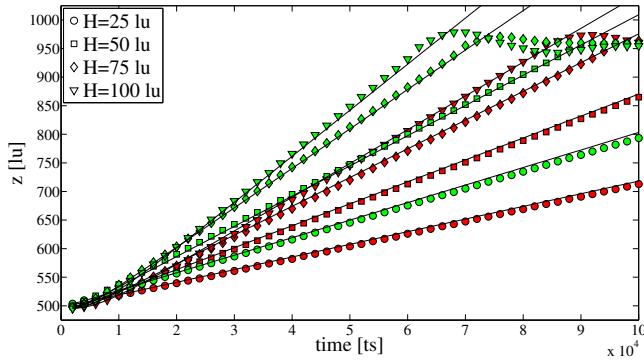


Figure 6: Liquid displacement inside the capillary versus time. Points represent the simulation results while the solid lines correspond to the theoretical prediction of Eq. 8. The data shown in red are obtained with the surface tension $\gamma = 0.12338 \text{ lu}\cdot\text{mu}/\text{ts}^2$ ($G_c = 0.8 \text{ lu}/\text{mu}/\text{ts}^2$). For the results displayed in green the surface tension is $\gamma = 0.16403 \text{ lu}\cdot\text{mu}/\text{ts}^2$ ($G_c = 0.9 \text{ lu}/\text{mu}/\text{ts}^2$). The length of the channels is $L = 500 \text{ lu}$. The results of the simulations are averaged over 10 frames.

to the proper definition and determination of the profile near the contact line (Huang et al., 2007). Figure 5 shows the invading front in the course of time for the system of Fig. 4. Agreement with the theoretical prediction is satisfactory, as shown in Fig. 6. Of course, the surface tension remains unchanged since it is not a property depending on the geometry of the system. It turns out that the dynamic contact angle is on average larger than the equilibrium contact angle. Figure

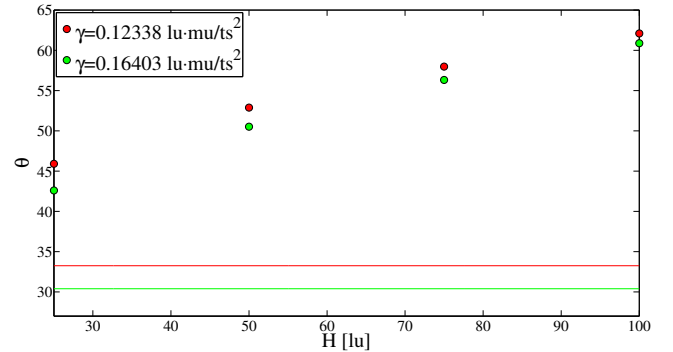


Figure 7: Dynamic contact angle, average value, as a function of the capillary width H (see Eq. 8). The solid lines represent the equilibrium contact angle as obtained using the sessile droplet system (see Sec. 3.2). The results are for channels of length $L = 500 \text{ lu}$.

7 indicates that the dynamic contact angle increases with H . Nevertheless, the process of infiltration is still faster for the capillaries of larger width (see Fig. 6). The present simulations are also repeated for $L = 750 \text{ lu}$ ($N_x = 1'500 \text{ lu}$) and $L = 1'000 \text{ lu}$ ($N_x = 2'000 \text{ lu}$) using similar systems. The results are not presented for brevity. The analysis leads to the same conclusions discussed so far.

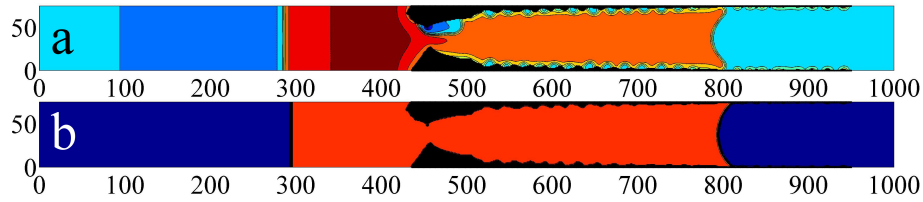


Figure 8: Typical interstice morphology as resulting from surface growth. The solid phase is represented in black. In red tonality the main component for mass transport and fluid flow. (a) Representation for solute concentration. (b) Representation for fluid density.

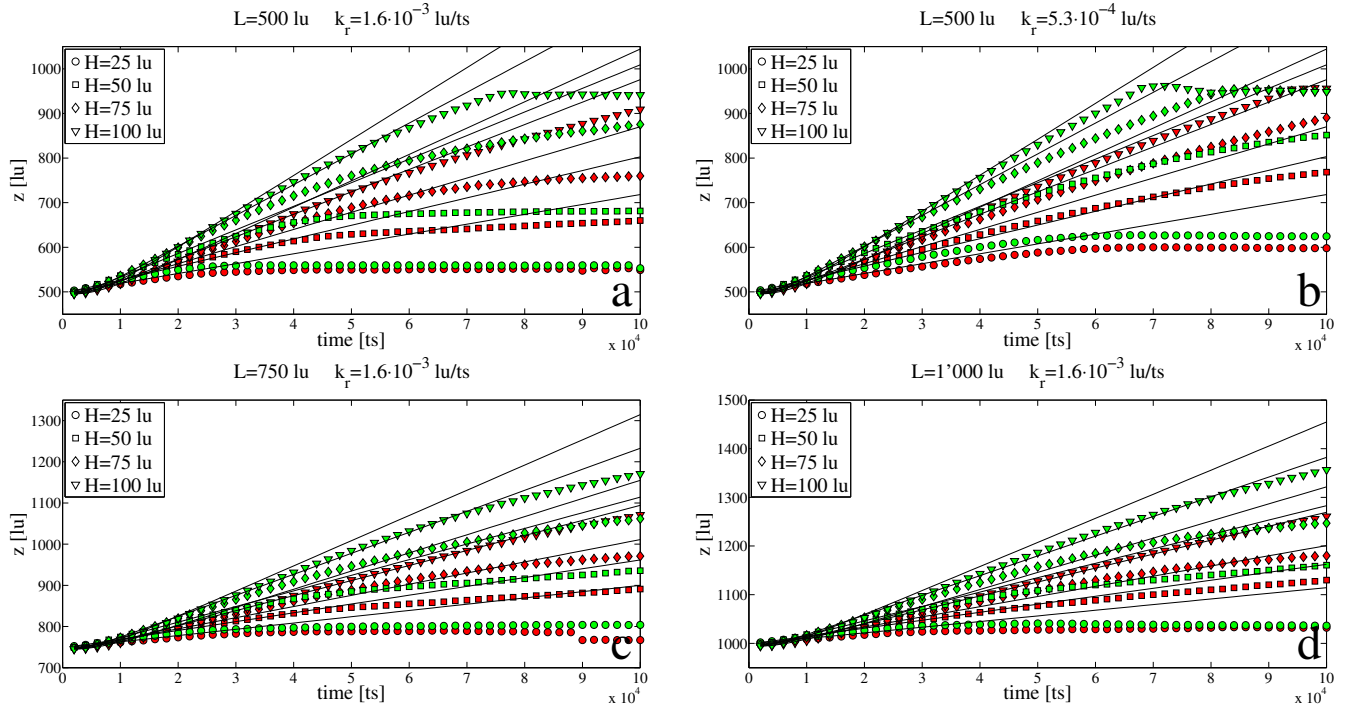


Figure 9: Time dependence of the infiltration depth with reactive boundaries. Data in red correspond to the surface tension $\gamma = 0.12338$ $\text{lu}\cdot\mu\text{u}/\text{ts}^2$ ($G_c = 0.8$ $\text{lu}/\mu\text{u}/\text{ts}^2$). The data represented in green refer to the surface tension $\gamma = 0.16403$ $\text{lu}\cdot\mu\text{u}/\text{ts}^2$ ($G_c = 0.9$ $\text{lu}/\mu\text{u}/\text{ts}^2$). The solid lines indicate the theoretical predictions in the absence of surface growth, Eq. 8.

3.4 Capillary infiltration with reactive boundaries

The SiC formation at the interface is responsible for wetting and spontaneous infiltration (Bougiouri et al., 2006). This process is not accounted for directly since our systems are composed by a wetting and a non-wetting fluid, separated by an interface. This means that in the present modeling scheme the reaction at the triple line and related phenomena are not taken into account (Calderon et al., 2010b; Dezellus et al., 2005; Voytovych et al., 2008). Furthermore, solute transport does not affect fluid flow. Since the fluid and the solute represent the same substance, it follows that fluid flow is influenced only by surface growth and not by the diffusion and precipitation processes. It is thus assumed that the amount of Si involved in the surface reaction is negligible with respect to the part regarded as a liquid.

The role of reactivity is investigated using again the setup illustrated in Fig. 4 in the course of evolutions totaling 100'000 timesteps. Regarding fluid flow, we consider all the

systems of Sec. 3.3 with the same initial conditions and the same settings defining the different wetting behaviors. For solute transport, in the initial condition, the region occupied by the wetting fluid is filled with solute at the concentration of $C_1 = 10^{-2}$ $\mu\text{u}/\text{lu}^2$. In the region occupied by the non-wetting fluid, the solute concentration is set to $C_2 = 2 \cdot 10^{-3}$ $\mu\text{u}/\text{lu}^2$. For the parameters of F_s , Eq. 3, we choose $G_s = -4.875 \cdot 10^{-3}$ $\mu\text{u}/\text{lu}/\text{ts}^2$, $\varphi_0 = 1$ and $C_0 = 4.9 \cdot 10^{-3}$ $\mu\text{u}/\text{lu}^2$. The saturated concentration is quite small compared to the bulk value of solute: it is chosen to be $C_s = 5 \cdot 10^{-3}$ $\mu\text{u}/\text{lu}^2$, determining the relative saturation $\psi = C_1/C_s = 2$. As a consequence, for relatively small values of k_r , the wetting fluid can be regarded as a reservoir for solute (Mortensen et al., 1997). Furthermore, these settings guarantee that in the non-wetting fluid, no solute deposits on the surface. The initial mass on solid boundaries is $b_0 = 2 \cdot 10^{-3}$ μu , and the threshold value for surface growth is assumed to be $b_{\max} = 10^{-2}$ μu . In order to adjust the effect of reaction relative to diffusion, it is sufficient to change the reaction-rate constant k_r , without varying the relaxation

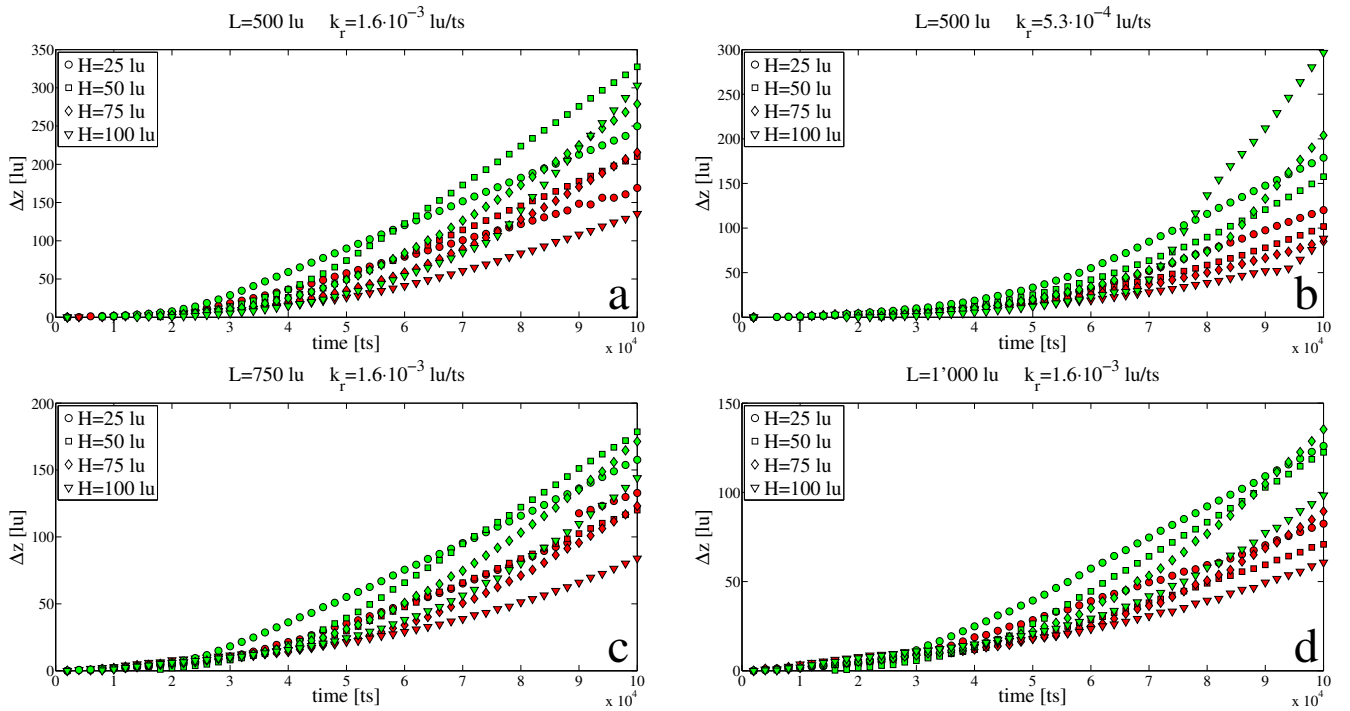


Figure 10: $\Delta z = z_t - z_r$ in the course of time. The lower script t refers to the theoretical value without reaction, Eq. 8; the symbol r indicates instead the front displacement for reactive boundaries. Red for data with surface tension $\gamma = 0.12338 \text{ lu}\cdot\mu\text{u}/\text{ts}^2$ ($G_c = 0.8 \text{ lu}/\mu\text{u}/\text{ts}^2$); green for data with surface tension $\gamma = 0.16403 \text{ lu}\cdot\mu\text{u}/\text{ts}^2$ ($G_c = 0.9 \text{ lu}/\mu\text{u}/\text{ts}^2$). It should be noted that linearity indicates that pore closure occurred in the case of reactive boundaries. This phenomenon is more frequent for narrow interstices. Another clear cause of linearity resides in the length of the capillary, that is, when the fluid reaches the other extremity in the absence of surface growth.

time for solute transport, set to $\tau_s = 1 \text{ ts}$ (Kang et al., 2003 and 2004). Indeed, the systems can be classified according to the relative saturation $\psi = C_1/C_s$ and the Damkohler number $Da = k_r N_y / D$. The reaction-rate constant is varied according to the rule $k_r = (8/5)/T$ with $T = 1'000, 2'000, \dots, 5'000 \text{ ts}$. Indicatively, this means that the flat surface start growing after 1'000, 2'000, \dots , 5'000 timesteps. Figure 8 shows a typical configuration. It can be seen that the solid phase grows especially near the capillary throat. As evidenced by Fig. 9, the invading front varies linearly with time also for reactive boundaries. We see that by varying γ , k_r and L the relative position between the various curves appears to be the same. This means that the hierarchy between the associated infiltration rates remains unchanged. It is of course necessary to take into account that narrow interstices obstruct sooner. In Fig. 10 we compare more closely the position of the invading front to the theoretical prediction in the absence of surface reaction, Eq. 8. The retardation in terms of distance is obtained by considering $\Delta z = z_t - z_r$; the lower scripts t and r stand for theoretical and reaction, specifying the two types of data. First of all, regarding the modeling approach, it is interesting to see that the curves corresponding to different surface tensions are separated more neatly. For the higher surface tension, more distance divides the invading front with reaction to that without reaction. Another general remark is that, for the wider and longer interstices, the retardation in terms of distance tends to increase faster and almost linearly towards the end of the sim-

ulations. According to this representation of the simulation results, long interstices seem to be the optimal configuration, but this is not true. For example, for $\gamma = 0.12338 \text{ lu}\cdot\mu\text{u}/\text{ts}^2$ and $H = 100 \text{ lu}$, the invading front spans the distance of 400 lu if $L = 500 \text{ lu}$ as opposed to approximately 300 lu if $L = 1'000 \text{ lu}$. Let us now consider the maximal width Δe of the solid phase in the channel. This quantity can not exceed $N_y/2$. This value corresponds to pore closure. Figure 11 substantiates the discussion in Kang et al. (2003) related to the effect of the fluid velocity on boundary reactivity. It arises that these curves primarily depend on the reaction-rate constant k_r . The surface tension γ and the length of the capillary L do not seem to affect significantly the quantity Δe . Curves for interstices with different width H differ appreciably only when pore obstruction occurs. As a result, the process of surface growth leading to pore closure appears to be independent of the infiltration velocity. Narrow capillaries are thus more subjected to closure and their infiltration velocities are also smaller. It follows that narrow interstices are particularly detrimental for reactive fluid flow. Figure 12 shows the maximal width of the solid phase resulting from surface growth as a function of the reaction-rate constant k_r with an average taken over the last five frames. Also with this representation it can be seen that in passing from $L = 500 \text{ lu}$ to $L = 1'000 \text{ lu}$ the data are grouped almost similarly, even though the velocity decreases significantly. The largest difference is observed for the systems with $k_r = 1.6 \cdot 10^{-3} \text{ lu}/\text{ts}$, $H = 50 \text{ lu}$ and $\gamma = 0.12338$

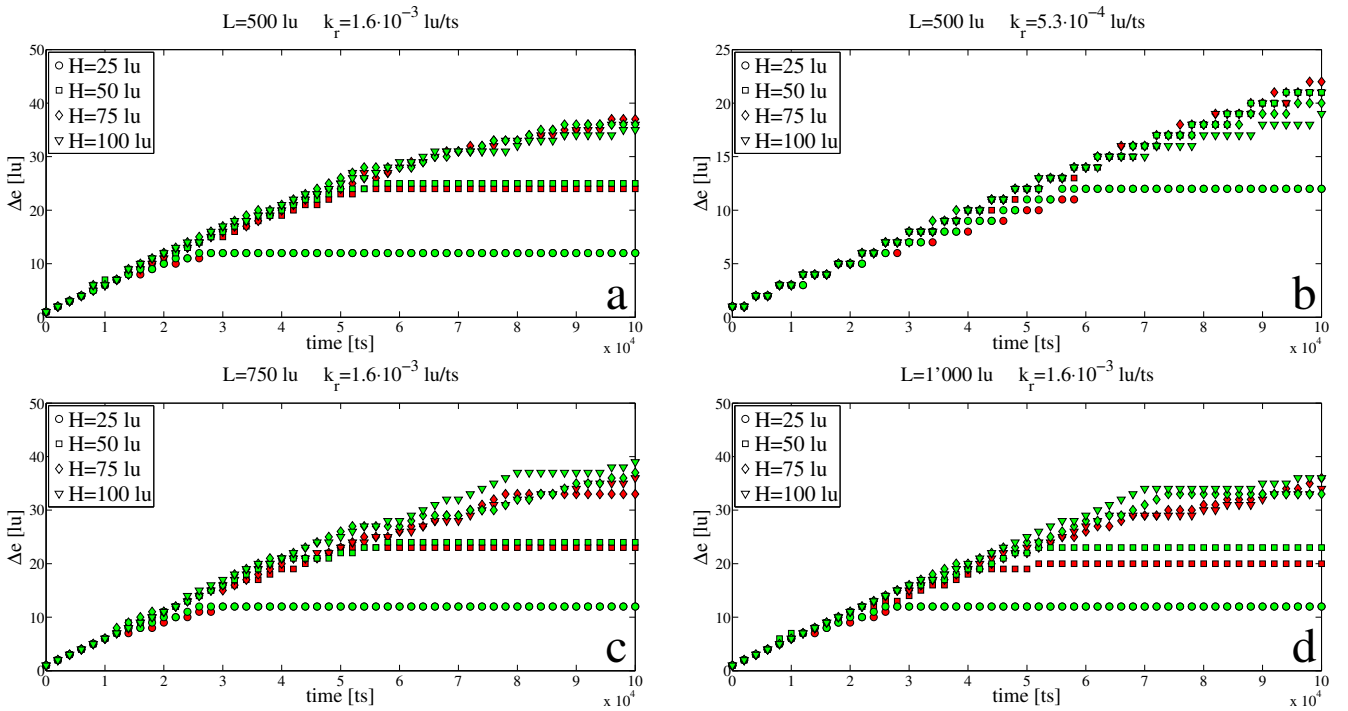


Figure 11: Time evolution of the maximal width Δe of the solid phase inside the capillary. Data in red have surface tension $\gamma = 0.12338$ $\text{lu}\cdot\text{mu}/\text{ts}^2$ ($G_c = 0.8$ $\text{lu}/\text{mu}/\text{ts}^2$); data in green have surface tension $\gamma = 0.16403$ $\text{lu}\cdot\text{mu}/\text{ts}^2$ ($G_c = 0.9$ $\text{lu}/\text{mu}/\text{ts}^2$).

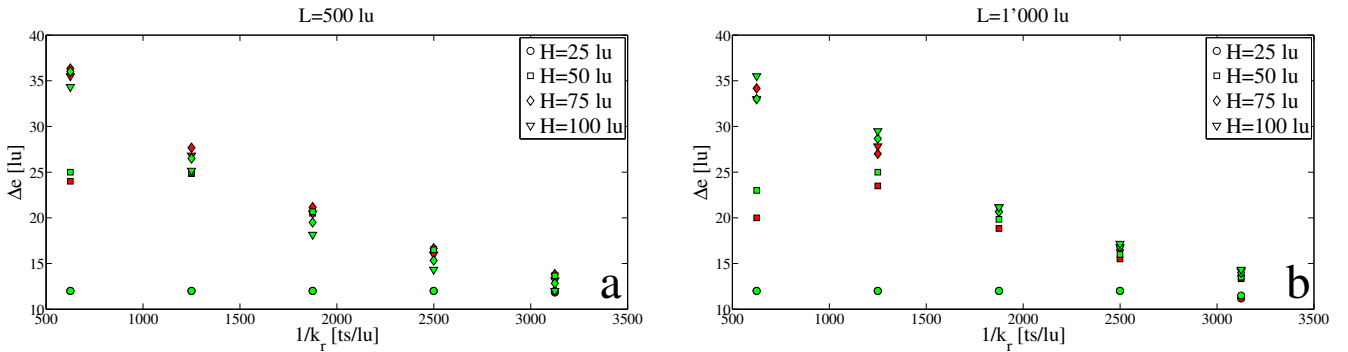


Figure 12: Maximal width Δe of the solid phase inside the capillary as a function of the reaction-rate constant k_r averaged over the last five frames. Data in red corresponds to the surface tension $\gamma = 0.12338$ $\text{lu}\cdot\text{mu}/\text{ts}^2$ ($G_c = 0.8$ $\text{lu}/\text{mu}/\text{ts}^2$); data in green are associated with the surface tension $\gamma = 0.16403$ $\text{lu}\cdot\text{mu}/\text{ts}^2$ ($G_c = 0.9$ $\text{lu}/\text{mu}/\text{ts}^2$).

$\text{lu}\cdot\text{mu}/\text{ts}^2$. For $L = 1'000$ lu , the quantity Δe only attains 20 lu . We consider this simulation an outlier. From Fig. 11 we see that for $L = 750$ lu pore closure occurs with $\Delta e = 23$ lu as for $L = 500$ lu .

4. Conclusions

In the present work we have studied through LB simulations in 2D the capillary infiltration in a single interstice with reactive boundaries. The complex process of liquid Si infiltration in C preforms was at the center of our attention. Severe inconsistencies exist between experimental and numerical conditions. For example, our models only reproduce

the expected macroscopic behavior for the infiltration. This means that the linear dependence on time arising from the reactivity (Bougiouri et al., 2006; Israel et al., 2010; Voytovych et al., 2008) is equivalent to the presence of a second fluid with the same density and viscosity as the reactive infiltrant component. In other words, our systems only reproduce the effective hydrodynamic behavior for the wetting fluid. In addition, our simulations overestimate the typical Reynolds numbers (Einset, 1996; Voytovych et al., 2008). In principle, the experimental conditions could be met with long channels. But from Fig. 11 we see that the length has little to no effect when the infiltration velocity is already small. In this work the focus is on a single capillary, but for interconnected porous systems the infiltration process turns out to be slower

(Einset, 1996). Another simplifying assumption is that the LB simulations are performed in the isothermal regime. It has been demonstrated that SiC formation is a highly exothermic reaction (Sangsuwan et al., 1999); moreover, spreading and infiltration appear to be quite sensitive to the temperature (Bougiouri et al., 2006). As a consequence, quantitative agreement is poor and it seems difficult to pinpoint the origin of inaccuracy given the mutual dependence of the various complex mechanisms at play. Furthermore, the Damkohler number Da is a free parameter in our simulations. In that respect, for interconnected porous systems, one way to establish a contact with the experimental results could be to consider the SiC formation at the droplet contact area when flow stops. The structural properties of the resulting surface should allow to choose more accurately the range of interest for the parameters controlling the reaction. Nevertheless, the proposed analysis still provides us with some guidance. In a real porous preform the pores have different sizes and thus the Damkohler number Da varies locally. This means that the SiC compound does not grow in the same way in all interstices. So, all our systems are representative for the problems of flow retardation and pore closure. It is found that the thickening behind the invading front effectively hinders the process of capillary infiltration. It turns out that wide and short interstices can limit the effect of pore closure (see Figs. 9 and 10). In other words, porous pathways as straight as possible should ease and dominate infiltration. Concerning the industrial manufacture of C/SiC composites (Krenkel, 2005), it follows that the most extended surface of the carbon matrix should be put in contact with molten Si, of course, if the porosity is isotropic. Then, surface growth does not result in a uniform corrugation of the initial flat surface but concentrates near the throat (see Fig. 8). Thus, another way to reduce the slow-down of reactive capillary infiltration could consist in having round-shaped morphologies for the structure of the porous medium. Importantly, narrow interstices are doubly disadvantageous since the process of pore closure can be regarded as independent of the infiltration velocity of fluid flow (see Fig. 11). In that respect, it is worth noticing that the benefits of bimodal distributions for pore size have been recognized in experimental investigations (Ortona et al., 2012). Similar conclusions were also reached in the seminal work of Messner and Chiang (1990). In their theoretical study, the invading front has a parabolic time dependence and the effects of surface reaction are introduced in an ad-hoc way (cf. Bougiouri et al. (2006)). Our next step would be to relate more tightly the coupled phenomena of the evolution of pore structure and capillary infiltration to the parameters controlling the porosity. The LB method has the advantage to offer a pore-scale description. This capability can enable an improvement of the manufacturing conditions of ceramic structures. To this end, possible extensions of our work may account for the structural features of single channels, pore connectivity and the packing structures of particles reproducing the porosity of the matrix.

Acknowledgments

The research leading to these results has received funding from the European Union Seventh Framework Programme (FP7/2007-2013) under grant agreement n° 280464, project "High-frequency ELectro-Magnetic technologies for advanced processing of ceramic matrix composites and graphite expansion" (HELM).

References

1. Benzi R, Succi S, Vergassola M (1992). The lattice Boltzmann equation: theory and applications. *Physics Reports* 222(3):145-197.
2. Bhatnagar P, Gross E, Krook A (1954). A model for collision processes in gases. I. Small amplitudes processes in charged and neutral one-component systems. *Physical Review* 94(3):511-525.
3. Bougiouri V, Voytovych R, Rojo-Calderon N, Narciso J, Eustathopoulos N (2006). The role of the chemical reaction in the infiltration of porous carbon by NiSi alloys. *Scripta Materialia* 54(11):1875-1878.
4. Calderon NR, Voytovych R, Narciso J, Eustathopoulos N (2010a). Pressureless infiltration versus wetting in AlSi/graphite systems. *Journal of Materials Science* 45(16):4345-4350.
5. Calderon NR, Voytovych R, Narciso J, Eustathopoulos N (2010b). Wetting dynamics versus interfacial reactivity of AlSi alloys on carbon. *Journal of Materials Science* 45(8):2150-2156.
6. Chen S, Doolen GD (1998). Lattice Boltzmann method for fluid flows. *Annual Review of Fluid Mechanics* 30:329-364.
7. Chibbaro S (2008). Capillary filling with pseudo-potential binary Lattice-Boltzmann model. *The European Physical Journal E* 27(1):99-106.
8. Chibbaro S, Biferale L, Diotallevi F, Succi S (2009a). Capillary filling for multicomponent fluid using the pseudo-potential Lattice Boltzmann method. *The European Physical Journal Special Topics* 171(1):223-228.
9. Chibbaro S, Costa E, Dimitrov DI, Diotallevi F, Milchev A, Palmieri D, Pontrelli G, Succi S (2009b). Capillary filling in microchannels with wall corrugations: A comparative study of the Concus-Finn criterion by continuum, kinetic, and atomistic approaches. *Langmuir* 25(21):12653-12660.
10. Dezellus O, Eustathopoulos N (2010). Fundamental issues of reactive wetting by liquid metals. *Journal of Materials Science* 45(16):4256-4264.

11. Dezellus O, Hodaj F, Eustathopoulos N (2003). Progress in modelling of chemical-reaction limited wetting. *Journal of the European Ceramic Society* 23(15):2797-2803.
12. Dezellus O, Jacques S, Hodaj F, Eustathopoulos N (2005). Wetting and infiltration of carbon by liquid silicon. *Journal of Materials Science* 40(9-10):2307-2311.
13. Diotallevi F, Biferale L, Chibbaro S, Lamura A, Pontrelli G, Sbragaglia M, Succi S, Toschi T (2009a). Capillary filling using lattice Boltzmann equations: The case of multi-phase flows. *The European Physical Journal Special Topics* 166(1):111-116.
14. Diotallevi F, Biferale L, Chibbaro S, Pontrelli G, Toschi F, Succi S (2009b). Lattice Boltzmann simulations of capillary filling: Finite vapour density effects. *The European Physical Journal Special Topics* 171(1):237-243.
15. Einset EO (1996). Capillary infiltration rates into porous media with application to silcomp processing. *Journal of the American Ceramic Society* 79(2):333-338.
16. Einset EO (1998). Analysis of reactive melt infiltration in the processing of ceramics and ceramic composites. *Chemical Engineering Science* 53(5):1027-1039.
17. Eustathopoulos N, Nicholas MG, Drevet B (1999). *Wettability at High Temperatures*, Pergamon.
18. de Gennes PG, Brochard-Wyart F, Quéré D (2004). *Capillarity and Wetting Phenomena: Drops, Bubbles, Pearls, Waves*, Springer.
19. He X, Luo LS (1997). A priori derivation of the lattice Boltzmann equation. *Physical Review E* 55(6):6333-6336.
20. Hillig WB, Mehan RL, Morelock CR, DeCarlo VJ, Laskow W (1975). Silicon/silicon carbide composites. *American Ceramic Society Bulletin* 54(12):1054-1056.
21. Huang H, Thorne DT, Shaap MG, Sukop MC (2007). Proposed approximation for contact angles in Shan-and-Chen-type multicomponent multiphase lattice Boltzmann models. *Physical Review E* 76(6):66701-66706.
22. Israel R, Voytovych R, Protsenko P, Drevet B, Camel D, Eustathopoulos N (2010). Capillary interaction between molten silicon and porous graphite. *Journal of Materials Science* 45(8):2210-2217.
23. Israelachvili JN (2011). *Intermolecular and Surface Forces*, Academic Press.
24. Kang Q, Lichtner PC, Zhang D (2007). An improved lattice Boltzmann model for multicomponent reactive transport in porous media at the pore scale. *Water Resources Research* 43:5551-5562.
25. Kang Q, Zhang D, Chen S (2003). Simulation of dissolution and precipitation in porous media. *Journal of Geophysical Research* 108(B10):2504-2513.
26. Kang Q, Zhang D, Chen S (2002a). Displacement of a two-dimensional immiscible droplet in a channel. *Physics of Fluids* 14(9):3203-3214.
27. Kang Q, Zhang D, Chen S, He X (2002b). Lattice Boltzmann simulation of chemical dissolution in porous media. *Physical Review E* 65(3):36318-36325.
28. Kang Q, Zhang D, Lichtner PC, Tsimpanogiannis IN (2004). Lattice Boltzmann model for crystal growth from supersaturated solution. *Geophysical Research Letters* 31:21107-21111.
29. Krenkel W (2005). Carbon fibre reinforced silicon carbide composites (C/SiC, C/C-SiC). *Handbook of Ceramic Composites*, Kluwer Academic Publisher, 117-48.
30. Landau LD, Lifshitz EM (2008). *Fluid Mechanics*, Elsevier.
31. Liu GW, Muolo ML, Valenza F, Passerone A (2010). Survey on wetting of SiC by molten metals. *Ceramics International* 36(4):1177-1188.
32. Lu G, DePaolo DJ, Kang Q, Zhang D (2009). Lattice Boltzmann simulation of snow crystal growth in clouds. *Journal of Geophysical Research* 114:11087-11100.
33. Lucas R (1918). Rate of capillary ascension of liquids. *Kolloid-Z* 23:15-22.
34. Martys NW, Chen HD (1996). Simulation of multicomponent fluids in complex three-dimensional geometries by lattice Boltzmann method. *Physical Review E* 53(1):743-750.
35. Miller W, Succi S (2002). A lattice Boltzmann model for anisotropic crystal growth from melt. *Journal of Statistical Physics* 107(1-2):173-186.
36. Messner RP, Chiang YM (1990). Liquid-phase reaction-bonding of silicon carbide using alloyed silicon-molybdenum melts. *Journal of the American Ceramic Society* 73(5):1193-1200.
37. Mohamad AA, El-Ganaoui M, Bennacer R (2009). Lattice Boltzmann simulation of natural convection in an open ended cavity. *International Journal of Thermal Sciences* 48(10):1870-1875.
38. Mohamad AA, Kuzmin A (2010). A critical evaluation of force term in lattice Boltzmann method, natural convection problem. *International Journal of Heat and Mass Transfer* 53(5-6):990-996.
39. Mortensen A, Drevet B, Eustathopoulos N (1997). Kinetics of diffusion-limited spreading of sessile drops in reactive wetting. *Scripta Materialia* 36(6):645-651.

40. Ortona A, Fino P, D'Angelo C, Biamino S, D'Amico G, Gaia D, Gianella S (2012). Si-SiC-ZrB₂ ceramics by silicon reactive infiltration. *Ceramics International* 38(4):3243-3250.
41. Pooley CM, Kusumaatmaja H, Yeomans JM (2009). Modelling capillary filling dynamics using lattice Boltzmann simulations. *The European Physical Journal Special Topics* 171(1):63-71.
42. Sangsuwan P, Tewari SN, Gatica JE, Singh M, Dickerson R (1999). Reactive infiltration of silicon melt through microporous amorphous carbon preforms. *Metallurgical and Materials Transaction B* 30B(5):933-944.
43. Schmieschek S, Harting J (2011). Contact angle determination in multicomponent lattice Boltzmann simulations. *Communications in Computational Physics* 9(5):1165-1178.
44. Sergi D, Scocchi G, Ortona A (2012). Molecular dynamics simulations of the contact angle between water droplets and graphite surfaces. *Fluid Phase Equilibria* 332:173-177.
45. Shan X, Chen H (1993). Lattice Boltzmann model for simulating flows with multiple phases and components. *Physical Review E* 47(3):1815-1819.
46. Shan X, Chen H (1994). Simulation of nonideal gases and liquid-gas phase transitions by the lattice Boltzmann equation. *Physical Review E* 49(4):2941-2948.
47. Shan X, Doolen GD (1995). Multicomponent lattice-Boltzmann model with interparticle interaction. *Journal of Statistical Physics* 81(1-2):379-393.
48. Succi S (2009). *The Lattice Boltzmann Equation for Fluid Dynamics and Beyond*, Oxford University Press.
49. Sukop MC, Thorne Jr DT (2010). *Lattice Boltzmann Modeling: An Introduction for Geoscientists and Engineers*, Springer.
50. Szekely J, Neumann AW, Chuang YK (1971). The rate of capillary penetration and the applicability of the Washburn equation. *Journal of Colloid and Interface Science* 35(2):273-278.
51. Voytovych R, Bougiouri V, Calderon NR, Narciso J, Eustathopoulos N (2008). Reactive infiltration of porous graphite by NiSi alloys. *Acta Materialia* 56(10):2237-2246.
52. Washburn EW (1921). The dynamics of capillary rise. *Physical Review* 27(3):273-283.
53. Wolf-Gladrow DA (2005). *Lattice-Gas Cellular Automata and Lattice Boltzmann Models - An Introduction*, Springer.
54. Wolf-Gladrow D (1995). A lattice Boltzmann equation for diffusion. *Journal of Statistical Physics* 79(5-6):1023-1032.
55. Young T (1805). An essay on the cohesion of fluids. *Philosophical Transactions of the Royal Society of London* 95:65-87.